Electrochemical Oxidation of Size-Selected Pt Nanoparticles Studied Using in Situ High-Energy-Resolution X-ray Absorption Spectroscopy

Lindsay R. Merte,[†] Farzad Behafarid,[†] Daniel J. Miller,[‡] Daniel Friebel,[‡] Sangwan Cho,[‡] Felix Mbuga,[§] Dimosthenis Sokaras,[§] Roberto Alonso-Mori,[‖] Tsu-Chien Weng,[§] Dennis Nordlund,[§] Anders Nilsson,*,[‡] and Beatriz Roldan Cuenya*,[†]

[†]Department of Physics, University of Central Florida, Orlando, Florida 32816, United States

[‡]Stanford Institute of Materials and Energy Science, [§]Stanford Synchrotron Radiation Lightsource, and [‖]Linac Coherent Light Source, SLAC National Accelerator Laboratory, Menlo Park, California 94025, United States

S *Supporting Information*

ABSTRACT: High-energy-resolution fluorescence-detected X-ray absorption spectroscopy (HERFD-XAS) has been applied to study the chemical state of ~1.2 nm size-selected Pt nanoparticles (NPs) in an electrochemical environment under potential control. Spectral features due to chemisorbed hydrogen, chemisorbed O/OH, and platinum oxides can be distinguished with increasing potential. Pt electro-oxidation follows two competitive pathways involving both oxide formation and Pt dissolution.
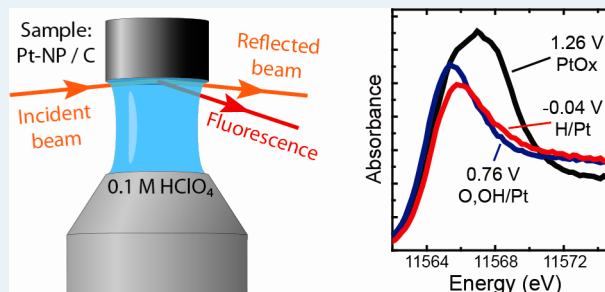
KEYWORDS: Pt, PtOx, nanoparticle, electrocatalysis, HERFD-XAS, XANES

1. INTRODUCTION

The oxidation behavior of Pt in electrochemical environments is of considerable technological interest, since the performance and long-term stability of low-temperature fuel cells are largely determined by surface processes occurring at oxidizing potentials at the Pt cathodes, for example, H_2O and O_2 adsorption and dissociation, oxide formation,[1,2] and Pt dissolution.[3−6] The influence of the nanoparticle (NP) size and structure on their oxidation behavior is also important, since high metal dispersion (i.e., small particle sizes) is mandated by the high cost of platinum.

Several studies have suggested that the specific activity (i.e., reaction rate per exposed surface atom) of Pt NPs toward the oxygen reduction reaction (ORR) decreases with decreasing NP size and drops precipitously below ~3 nm.[7−19] Nevertheless, because the proportion of accessible Pt sites increases with decreasing size, the mass activity assumes a maximum at ~2−4 nm NP size. This phenomenon, which limits the degree to which catalysts can be dispersed, possibly arises from the stronger binding of oxygen to smaller NPs.[20,21] In particular, higher surface concentrations of chemisorbed OH, O, or PtO_x species may hinder the reduction of O_2.[21,22]

Knowledge of the chemical state of Pt under oxidizing conditions is needed for an understanding of the degradation of fuel cell performance during long-term operation, due primarily to the loss of electrocatalytic surface area at the cathode at high potentials. Several degradation mechanisms have been proposed and discussed somewhat controversially, in particular, Pt dissolution,[3,4] corrosion of the carbon support,[23] detachment of entire particles,[24] and NP growth via Ostwald ripening or agglomeration.[3,4,23] Instead of contributing to Ostwald ripening, dissolved Pt species can also be trapped in the polymer membrane, where they cannot participate in the electrochemical cycle.[5] These effects depend on NP size: more extensive dissolution and coarsening is observed with decreasing NP size.[4]

The mechanism by which the oxidation state of Pt affects cathode degradation is still not well understood. Some reports assign the stabilization of Pt NPs against dissolution to the formation of a passivating surface-oxide layer at the highest potentials,[25,26] whereas a more rapid Pt dissolution was observed at intermediate potentials,[6,26] where the NP surfaces are only partly oxidized.[26,27] These studies furthermore suggest that NP stability depends on the rates of Pt oxidation and reduction,[26,27] which can be externally controlled using different voltage sweeps. The degradation of Pt NPs might therefore be influenced not only by their overall oxidation state, but also by their surface morphology and structural order.[28]

To elucidate the relationship between the structure and operational characteristics of a nanosized electrocatalyst, one must study well-defined samples in situ under operating conditions. Here, we present an in situ study of the chemical state of size-selected Pt NPs on a glassy carbon (GC) support

using high-energy-resolution fluorescence-detected X-ray absorption spectroscopy (HERFD-XAS) at the Pt L_3 edge.

2. EXPERIMENTAL SECTION

2.1. Sample Preparation. Two samples with different average NP size distributions were prepared by dissolving H_2PtCl_6 into polystyrene-*b*-poly(2-vinylpyridine) polymeric solutions [PS(16000)-*b*-P2VP(3500) in toluene] containing inverse micelles.[37] The Pt salts were added to the solutions in a nitrogen-flushed glovebox, and the quantities of Pt added, which determined the final sizes of the Pt NPs, were chosen to give metal-to-P2VP ratios of 0.1 (sample S1) and 0.05 (sample S2). The solutions were stirred for 2 days at room temperature to ensure complete dissolution of the H_2PtCl_6 into the micelles. Subsequently, the solutions were dip-coated onto SiO_2(4 nm)/Si(111) wafers (used for AFM imaging) and onto polished glassy carbon disks (for XAS measurements). The polymer shells were then removed using an ultrahigh vacuum oxygen plasma source (SPECS, GmbH), which leaves behind oxidized platinum NPs.[20,38]

2.2. Sample Characterization. X-ray photoelectron spectroscopy (XPS) measurements were performed in normal emission using a monochromatic Al-Kα (1486.6 eV) X-ray source and a hemispherical energy analyzer (Phoibos, SPECS GmbH) with a fixed pass energy of 18 eV. Binding energies are referenced to the C 1s photoemission line of glassy carbon (283.9 eV). Using the least-squares fitting routine in the CasaXPS program, Pt 4f spectra were deconvolved into peaks corresponding to Pt^{2+} in PtO (72.29 eV for $4f_{7/2}$) and Pt^{4+} in PtO_2 (73.89 eV $4f_{7/2}$). The positions of the Pt $4f_{7/2}$ peaks were allowed to vary, while the magnitude of the spin−orbit splitting, ΔE, between the $4f_{7/2}$ and $4f_{5/2}$ peaks was fixed at +3.33 eV. Asymmetric modified Gaussian−Lorentzian (G-L) line shapes were used, with full-widths at half-maximum of 2.0 eV (fitted) for Pt^{2+} and 1.5 eV (fitted) for Pt^{4+}. The $4f_{5/2}$:$4f_{7/2}$ intensity ratios were fixed at 0.75. Adding metallic (Pt^0) components at 71.0 and 74.3 eV did not improve the quality of the fits, corroborating the oxidized state of the as-prepared sample.

Atomic force microscopy (AFM) images were obtained in tapping mode with a Veeco Multimode AFM and Si tips. Particle heights were determined from line profiles measured across individual NPs.

2.3. In Situ XAS Measurements. The electrochemical cell used for the in situ measurements consists of a PEEK tube that contains the electrolyte, a counter electrode (glassy carbon) and an Ag/AgCl reference electrode. Contact with the working electrode is established through a free-standing meniscus in the ~2 mm gap between the tube and the sample surface.[33,34] A 0.1 M $HClO_4$ electrolyte was made from 70% $HClO_4$ (Trace Select Ultra, Sigma-Aldrich) and ultrapure water from a Millipore Gradient system. All potentials were converted to the scale of the reversible hydrogen electrode (RHE) using the measured onset of H_2 evolution on the sample surface.

The HERFD-XAS spectra were acquired at beamline 6-2 at the Stanford Synchrotron Radiation Laboratory (SSRL) using a Si(111) monochromator in combination with a Rowland circle analyzer spectrometer comprising five spherically bent Ge perfect crystals (R = 1 m). The crystals were aligned in a backscattering geometry using the (660) Bragg reflection at 80.0° to select the Pt Lα_1 fluorescence line (9442 eV). The combined resolution of the monochromator and analyzer determined by measuring the elastic scattering was 1.6 eV. The sample was aligned in grazing incidence, with the electric field

vector oriented parallel to the surface. The incident photon energy was calibrated using the transmission-mode XAS spectrum of a Pt foil placed in the beam after the sample. A value of 11564 eV was assigned to the inflection point of the leading edge of the Pt foil spectrum. HERFD-XAS measurements were obtained for both samples S1 and S2 in the as-prepared state with the electrochemical cell flushed with dry N_2. In situ electrochemical measurements were performed only on sample S1.

In HERFD-XAS,[29−31] the effective core−hole lifetime is significantly reduced compared to conventional XAS. Since absorption at the Pt L_3 edge excites 2p electrons to either a single resonance associated with 5d holes or to s and d continuum states, the sole effect of HERFD-XAS when applied at the Pt L_3 edge is to sharpen features observed in conventional XAS. In particular, changes in the near-edge absorption maximum or "white line" can be resolved more clearly. The "white-line" at the Pt L_3 edge arises from $2p_{3/2}$ to 5d transitions, and its intensity has been shown to be proportional to the unoccupied 5d electron density of states,[32] which is very sensitive to changes in the chemical environment of the Pt atoms. Chemisorbed oxygen species and Pt oxides are therefore more readily distinguished using HERFD-XAS than with conventional XAS.[29,33−36]

The X-ray absorption near edge spectra (XANES) were fitted using a sum of two pseudo-Voigt (Gaussian−Lorentzian product) peaks (eq 1) after subtraction of a background consisting of an arctangent function (eq 2):

$$\frac{A_n}{1 + 4 \cdot m_n \frac{(E - E_n)^2}{\Delta E_n^2}} \cdot \exp\left[-4 \cdot \ln 2 \cdot (1 - m_n) \cdot \frac{(E - E_n)^2}{\Delta E_n^2}\right]$$

(1)

$$\frac{A_{bg}}{\pi}\left[\tan^{-1}\left(\frac{E - E_{bg}}{\Delta E_{bg}}\right) + \frac{\pi}{2}\right]$$

(2)

The height of the arctan jump (A_{bg}) was varied to match the value of $\mu(E)$ at energies between 11572 and 11574 eV, while its position (E_{bg}) and width (ΔE_{bg}) were fixed. The parameters which were allowed to vary were the heights (A_1, A_2) and FWHM's ($\Delta E_1, \Delta E_2$) of both peaks. The G-L mixing proportions (m_1, m_2) and peak positions (E_1, E_2) were fixed, except at −0.04 and 0.16 V, where E_1 was allowed to vary to account for the hydrogen-induced shift in the white-line.

3. RESULTS AND DISCUSSION

The sizes of the NPs used to prepare sample S1 were determined by AFM [Figure 1a] using a flat SiO_2/Si(111) wafer as a substrate, since the NPs were too small to be imaged on the rougher GC surface used in the electrochemical experiments. The observed size distribution shows a mean NP height of 1.2 nm with a standard deviation of 0.4 nm [Figure 1b]. AFM measurements were also made for sample S2 (not shown), and though the particles were detectable, the roughness of the underlying silicon wafer (~0.5 nm rms) was too high to quantify the particle heights accurately. The particles were clearly smaller than those of S1, however, and the majority appeared to be <1 nm in height.

Pt 4f XPS spectra shown in Figure 2 reveal that the as-prepared, GC-supported NPs exist primarily in the 4+ oxidation state, that is, as PtO_2.[20,38] There is a dominant Pt $4f_{7/2}$ peak at 73.9 eV arising from PtO_2, and a minor
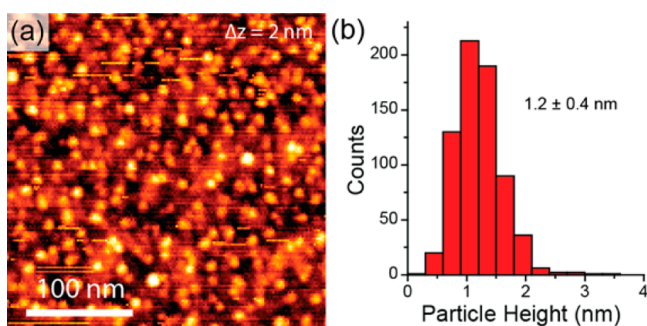
Figure 1. (a) AFM image of micelle-synthesized Pt NPs on SiO$_2$/Si(111) (S1) acquired after polymer removal by an O$_2$-plasma. (b) Distribution of Pt NP heights extracted from AFM measurements.
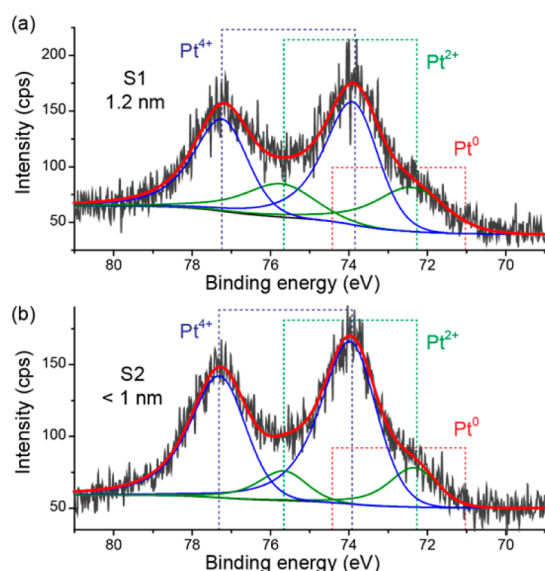

Figure 2. XPS spectra of two Pt NP on GC samples prepared using different micellar solutions leading to distinct average NP size distributions. (a) S1 (~1.2 nm), which was used for the electrochemical experiments reported here. (b) S2 (<1 nm).

contribution at 72.3 eV due to Pt^{2+} (PtO), but no detectable Pt^0. When comparing two samples with different average NP size distributions, the largest initial content of PtO$_2$ species was observed for the smaller NPs: sample S2 comprises 83% PtO$_2$ and 17% PtO, versus 68% PtO$_2$ and 32% PtO for sample S1. The HERFD-XAS spectrum of the as-prepared sample S1, which was recorded in an atmosphere of dry N$_2$ [see Figure 3a and Figure 4a], is accordingly similar to previous HERFD-XAS measurements of highly oxidized platinum NPs and thin films.[34,39,40] The corresponding spectrum of the as-prepared sample S2 (to be discussed below, see Figure 5) showed an even more intense white line, consistent with the greater proportion of Pt^{4+} observed in XPS.

To characterize the chemical states of the GC-supported NPs under electrochemical conditions, sample S1 was loaded into the hanging-meniscus electrochemical cell,[33,34] which allowed us to probe the sample surface with hard X-rays at grazing incidence while in contact with 0.1 M aqueous HClO$_4$. The sample was first exposed to the electrolyte while holding the potential at −0.04 V. Spectra were acquired consecutively at this potential until the signal stabilized and the Pt NPs were completely reduced. The potential was subsequently increased to +1.26 V in steps of 100 or 200 mV; HERFD-XAS spectra were acquired at each potential. The spectra obtained during this anodic sweep are shown in Figures 3a and 3b, respectively. As the potential is increased from −0.04 to 1.06 V, the main Pt L$_3$ edge absorption resonance or "white line" becomes narrower and more intense, and shifts by ~0.5 eV to lower energy. From 0.96 to 1.26 V, the white line broadens substantially and shifts to higher energy by ~1 eV.

The broadening of the Pt white line, which begins at 0.96 V, originates from the formation of platinum oxides.[33,34] Most of the broadening occurred within the narrow potential interval from 1.06 to 1.16 V. Oxide formation at 1.16 V was followed with individual XAS scans on a time-scale of ~35 min [Figure 3 b]. To describe the potential-dependent changes of the white-line shape and intensity in a simple manner, the spectra were deconvolved using an arctangent function to describe the absorption edge jump and two symmetric pseudo-Voigt peaks, one at lower and one at higher energy. In the following, we refer to these peaks as "metallic" and "oxidic" components,
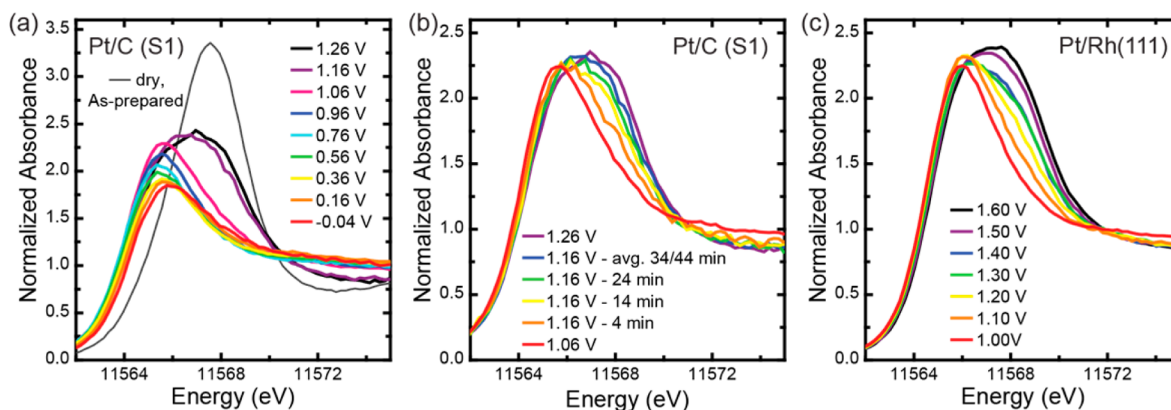

Figure 3. Pt L$_3$ HERFD-XAS spectra of Pt NPs on glassy carbon (S1) and of Pt islands on Rh(111) under potential control in contact with a 0.1 M HClO$_4$ electrolyte. (a) Spectra obtained from sample S1 after establishment of a steady state as the potential was increased in steps from −0.04 to 1.26 V. The spectrum of the as-prepared sample obtained in dry N$_2$ before contacting the electrolyte is shown for reference. (b) Time evolution of the spectrum of sample S1 while the potential was held at 1.16 V. Spectra at 1.06 and 1.26 V are shown for comparison, and the average of spectra obtained after 34 and 44 min represents the steady state at this potential. (c) HERFD-XAS of electrochemically prepared Pt islands on Rh(111).[33,35] In comparison with size-selected Pt NPs, significantly higher potentials are needed to achieve a similar amount of oxide formation.
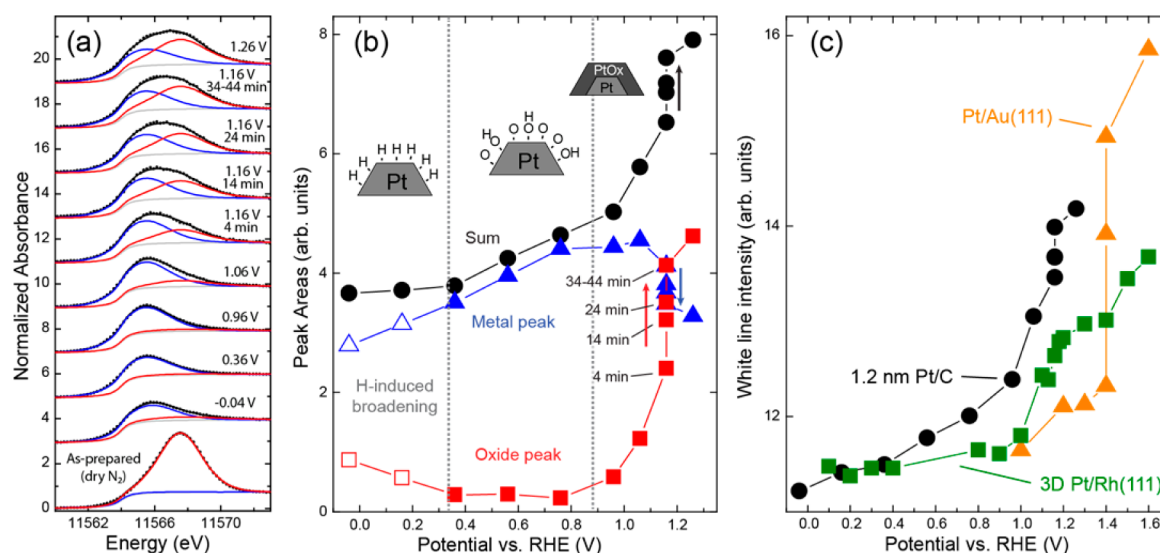
Figure 4. (a) Least-squares fits to selected XANES spectra from S1. (b) Areas of the fitted components for the full set of spectra acquired for S1, as well as their sum, plotted as a function of the sample potential. (c) HERFD-XAS white line intensities extracted by direct integration for Pt NPs on C (S1) as well as Pt/Au(111) and Pt/Rh(111) samples studied previously.[33]
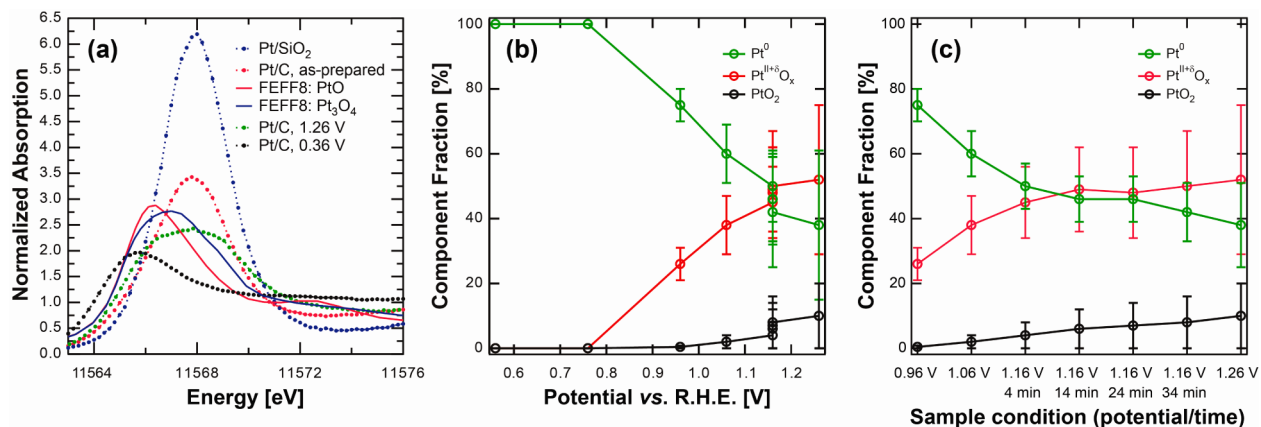

Figure 5. (a) Pt L_3 XANES spectra of as-prepared (oxidized) Pt NP samples in their dry state (~1.2 nm NPs on GC in S1 and <1 nm NPs on SiO₂ in S2) as well as the PtO and Pt_3O_4 spectra calculated using the FEFF8 code, and spectra of sample S1 under electrochemical conditions at 0.36 and 1.26 V. All potentials are reported versus R.H.E. Estimated potential- (b) and time-dependent (c) composition of Pt NPs in S1 during electrochemical Pt oxide formation.

respectively, since Pt metal and Pt oxide spectra are largely dominated by the respective peaks [see reference XANES spectra in Figure 5a]. However, a minor amount of the high-energy peak is needed throughout the potential range where Pt is purely in the metallic state (−0.04 to 0.76 V) to account for the asymmetry of the white-line shape. This effect is most pronounced at the lowest potentials and arises from hydrogen chemisorption, which is known to lead to a high-energy shoulder in XANES spectra.[44−46] As shown in Figure 4a, good fits could be obtained for all spectra from 0.56 to 1.26 V, as well as for the dry, as-prepared sample, by allowing only the peak heights and widths of the metallic and oxidic components to vary. The positions of the metal and oxide peaks and the position and width of the arctangent function were fixed in all fits. Because of the H-induced energy shift and broadening, the position of the metallic peak had to be varied to fit the spectra obtained at −0.04 and 0.16 V. Results of these fits can be found in the Supporting Information, Table S1.

The areas of the fitted metallic and oxidic components, as well as their sums, are plotted in Figure 4b as a function of

applied potential. The sum of the individual peak areas can be compared to the "integrated white-line intensity" often used in conventional XANES to indicate Pt oxidation state.[41−43] The broad high-energy shoulder observed in the spectra obtained at low potentials (−0.04 to +0.2 V) arises from chemisorbed hydrogen[44−46] [open symbols in Figure 4b], and completely disappears at +0.36 V. Between +0.36 and +0.76 V, the intensity of the oxide component is essentially negligible, while the metallic component grows steadily without shifting in energy, which is characteristic of an increasing coverage of chemisorbed oxygen species on the surface of the NPs. Previous FEFF[47] calculations of adsorbate structures on 1 ML Pt/Rh(111) showed little difference between the HERFD-XAS signatures of chemisorbed O and OH,[34] so we refer to it simply as chemisorbed O/OH. The oxide component first appears at 0.96 V, and increases most markedly while holding the potential at 1.16 V, see Figure 3b. Only a small additional increase in the intensity occurs upon further increasing the potential to 1.26 V, where it appears to approach an upper limit. At the same time, the intensity of the metal component

decreases, consistent with the conversion of metallic Pt to PtO_x. Although the oxide component of the sample in the electrolyte appears at the same energy as that of the dry, as-prepared sample, which consists mostly of PtO_2, it is somewhat broader (3.9 eV vs 3.2 eV FWHM). In addition, the peak intensity of the white line appears to saturate at a much lower value than that of the PtO_2-rich, as-prepared sample, indicating the presence of Pt in oxidation states lower than 4+, for example, 2+ (as found in PtO).

An accurate interpretation of the above spectra is challenging because of the lack of high-purity experimental standards for Pt oxides and the large uncertainty of the absolute energy scale in FEFF calculations. Nevertheless, to assess the composition of the NPs during electrooxidation, linear-combination fits were performed over an energy range from 11556.2 to 11585.3 eV using as standards the measured spectrum at 0.36 V for Pt metal, FEFF8 simulations for PtO and Pt_3O_4, and the measured spectrum of an as-prepared $SiO_2/Si(111)$-supported Pt NP sample (<1 nm NPs, sample S2) as an approximation for PtO_2, Figure 5a. Since multiple-scattering calculations can give large errors of up to 10 eV for the position of the spectrum on an absolute energy scale, the theoretical PtO and Pt_3O_4 standards were first shifted to have their first inflection point approximately halfway in between those of Pt and PtO_2, and their energy offsets were allowed to float in the fit at 1.26 V. The energy shifts obtained in this way were then kept constant while fitting all the other spectra. Eventually, three different sets of linear-combination fits were obtained, using as components either $Pt/PtO/PtO_2$, $Pt/PtO/Pt_3O_4$, or Pt/Pt_3O_4. Since we do not have further evidence that would lead us to favor one of the three fits, and because of the structural similarities between PtO and Pt_3O_4, we merged the three series by considering the individual coefficients for PtO and Pt_3O_4 as one coefficient for $Pt^{2+\delta}O_x$. The average of the highest and lowest coefficient for each of the species Pt, $Pt^{2+\delta}O_x$, and PtO_2 from the three series was then used as the coefficient in the merger, and half of the difference between the highest and lowest coefficient for each species was used to estimate the uncertainty. The results of these fits are summarized in Figures 5b,c and the fit details are shown in the Supporting Information, Table S2. This analysis using different combinations of phases at 1.26 V suggests that 0−20% of the Pt atoms in S1 may be present as PtO_2, up to 75% exist as PtO or Pt_3O_4, and 25−50% of the total XAS signal is due to Pt atoms remaining in the metallic state.

The GC-supported Pt NPs examined here appear to exhibit an onset potential for oxide formation that is somewhat lower than the value identified for electrochemically deposited Pt overlayers on Rh(111) (~1.0 V), which have also been studied using HERFD-XAS.[33,35] Moreover, the growth of Pt oxide in the present case is much more rapid. In particular, an almost identical shape of the white line as what is seen with Pt/Rh(111) at 1.6 V, Figure 3c, is already reached for our size-selected 1.2 nm NPs at 1.26 V, Figure 3a. This difference is most likely due to the stronger interactions between Pt and the Rh support, where the compression of the Pt lattice results in a decrease in the strength of the O/Pt binding and an increase in the energy barrier for O atoms to reach subsurface sites. Moreover, an increase in the metallic cohesion energy induced by Pt−Rh interactions apparently prevents dissolution of Pt, thus allowing only for the Pt/O place-exchange pathway[48] to contribute to Pt oxide growth. Pt dissolution does occur, in contrast, in carbon-supported Pt NPs at high potentials[3−6] and was also observed in a Pt/Au(111) model catalyst.[26] In the latter case, an alternative, more rapid pathway for Pt oxide formation through a dissolution−precipitation mechanism might be dominant. A comparison of the white line intensities (determined by direct integration of HERFD-XAS spectra between 11555 and 11571 eV) of 1.2 nm Pt/C, electrochemically prepared Pt/Au(111) and Pt/Rh(111) samples as a function of electrochemical potential is shown in Figure 4c.

In our study, the magnitude of the Pt fluorescence signal, determined primarily by the Pt mass loading of the sample, was observed to decrease over the course of the experiments, suggesting dissolution of Pt to some extent. The fact that the Pt did not dissolve completely suggests that the formation of a PtO_x shell could passivate the NPs[25,49] and that dissolution might occur most rapidly when the particles are only partially oxidized.

4. CONCLUSIONS

Our experiments revealed that the chemical state of Pt NPs on glassy carbon in 0.1 M $HClO_4$ can be divided into three distinct potential regimes: hydrogen chemisorption between 0 V and ~0.3 V, oxygen chemisorption (as OH or O) between 0.3 and 0.96 V, and platinum oxide formation at or above 0.96 V. Since the small NPs bind oxygen more strongly and form oxides more readily, these results suggest that to ensure not only high reactivity, but also long-term stability of Pt/C fuel cell cathode electrocatalysts, a compromise must be made between maximizing the number of active surface sites (e.g., by decreasing the NP size and increasing the surface-to-volume ratio) while minimizing Pt dissolution processes typical of small NPs such as the ones investigated here.

■ ASSOCIATED CONTENT

Ⓢ Supporting Information

Tables S1 and S2: results of peak fitting and linear combination fitting of XANES data acquired under potential control. This material is available free of charge via the Internet at http://pubs.acs.org.

■ AUTHOR INFORMATION

Corresponding Author

*E-mail: roldan@ucf.edu (B.R.C.), nilsson@slac.stanford.edu (A.N.).

Notes

The authors declare no competing financial interest.

■ ACKNOWLEDGMENTS

■ REFERENCES

(1) Conway, B. E. *Prog. Surf. Sci.* **1995**, *49*, 331−452.
(2) Jerkiewicz, G.; Vatankhah, G.; Lessard, J.; Soriaga, M. P.; Park, Y.-S. *Electrochim. Acta* **2004**, *49*, 1451−1459.

(3) Holby, E. F.; Sheng, W.; Shao-Horn, Y.; Morgan, D. *Energy Environ. Sci.* **2009**, *2*, 865−871.

(4) Shao-Horn, Y.; Sheng, W. C.; Chen, S.; Ferreira, P. J.; Holby, E. F.; Morgan, D. *Top. Catal.* **2007**, *46*, 285−305.

(5) Ferreira, P. J.; la O', G. J.; Shao-Horn, Y.; Morgan, D.; Makharia, R.; Kocha, S.; Gasteiger, H. A. *J. Electrochem. Soc.* **2005**, *152*, A2256.

(6) Wang, X.; Kumar, R.; Myers, D. *J. Electrochem. Solid-State Lett.* **2006**, *9*, A225.

(7) Antoine, O.; Bultel, Y.; Durand, R. *J. Electroanal. Chem.* **2001**, *499*, 85−94.

(8) Greeley, J.; Rossmeisl, J.; Hellmann, A.; Nørskov, J. K. *Z. Phys. Chem.* **2007**, *221*, 1209−1220.

(9) Tritsaris, G.; Greeley, J.; Rossmeisl, J.; Nørskov, J. K. *Catal. Lett.* **2011**, *141*, 909−913.

(10) Blurton, K. F.; Greenberg, P.; Oswin, H. G.; Rutt, D. R. *J. Electrochem. Soc.* **1972**, *119*, 559−564.

(11) Gasteiger, H. A.; Kocha, S. S.; Sompalli, B.; Wagner, F. T. *Appl. Catal., B* **2005**, *56*, 9−35.

(12) Kabbabi, A.; Gloaguen, F.; Andolfatto, F.; Durand, R. *J. Electroanal. Chem.* **1994**, *373*, 251−254.

(13) Kinoshita, K. *J. Electrochem. Soc.* **1990**, *137*, 845−848.

(14) Mukerjee, S. *J. Appl. Electrochem.* **1990**, *20*, 537−548.

(15) Peuckert, M.; Yoneda, T.; Dalla Betta, R. A.; Boudart, M. *J. Electrochem. Soc.* **1986**, *113*, 944−947.

(16) Rao, C. V.; Viswanathan, B. *J. Phys. Chem. C* **2010**, *114*, 8661−8667.

(17) Shao, M.; Peles, A.; Shoemaker, K. *Nano Lett.* **2011**, *11*, 3714−3719.

(18) Yahikozawa, K.; Fujii, Y.; Matsuda, Y.; Nishimura, K.; Takasu, Y. *Electrochim. Acta* **1991**, *36*, 973−978.

(19) Perez-Alonso, F. J.; McCarthy, D. N.; Nierhoff, A.; Hernandez-Fernandez, P.; Strebel, C.; Stephens, I. E. L.; Nielsen, J. H.; Chorkendorff, I. *Angew. Chem., Int. Ed.* **2012**, *51*, 4641−4643.

(20) Ono, L. K.; Croy, J. R.; Heinrich, H.; Roldan Cuenya, B. *J. Phys. Chem. C* **2011**, *115*, 16856−16866.

(21) Mayrhofer, K. J. J.; Blizanac, B. B.; Arenz, M.; Stamenkovic, V. R.; Ross, P. N.; Markovic, N. M. *J. Phys. Chem. B* **2005**, *109*, 14433−14440.

(22) Mukerjee, S.; McBreen, J. *J. Electroanal. Chem.* **1998**, *448*, 163−171.

(23) Meier, J. C.; Galeano, C.; Katsounaros, I.; Topalov, A. A.; Kostka, A.; Schüth, F.; Mayrhofer, K. J. J. *ACS Catal.* **2012**, *2*, 832−843.

(24) Mayrhofer, K. J. J.; Meier, J. C.; Ashton, S. J.; Wiberg, G. K. H.; Kraus, F.; Hanzlik, M.; Arenz, M. *Electrochem. Commun.* **2008**, *10*, 1144−1147.

(25) Darling, R. M.; Meyers, J. P. *J. Electrochem. Soc.* **2003**, *150*, A1523−A1527.

(26) Mitsushima, S.; Kawahara, S.; Ota, K.-i.; Kamiya, N. *J. Electrochem. Soc.* **2007**, *154*, B153−B158.

(27) Kinoshita, K.; Lundquist, J. T.; Stonehart, P. *J. Electroanal. Chem.* **1973**, *48*, 157−166.

(28) Mostafa, S.; Behafarid, F.; Croy, J. R.; Ono, L. K.; Li, L.; Yang, J. C.; Frenkel, A. I.; Roldan Cuenya, B. *J. Am. Chem. Soc.* **2010**, *132*, 15714−15719.

(29) de Groot, F. M. F.; Krisch, M. H.; Vogel, J. *Phys. Rev. B* **2002**, *66*, 195112.

(30) Glatzel, P.; Bergmann, U. *Coord. Chem. Rev.* **2005**, *249*, 65−95.

(31) Hämäläinen, K.; Siddons, D. P.; Hastings, J. B.; Berman, L. E. *Phys. Rev. Lett.* **1991**, *67*, 2850−2853.

(32) Qi, B.; Perez, I.; Ansari, P. H.; Lu, F.; Croft, M. *Phys. Rev. B* **1987**, *36*, 2972−2975.

(33) Friebel, D.; Miller, D. J.; Nordlund, D.; Ogasawara, H.; Nilsson, A. *Angew. Chem., Int. Ed.* **2011**, *50*, 10190−10192.

(34) Friebel, D.; Miller, D. J.; O'Grady, C. P.; Anniyev, T.; Bargar, J.; Bergmann, U.; Ogasawara, H.; Wikfeldt, K. T.; Pettersson, L. G. M.; Nilsson, A. *Phys. Chem. Chem. Phys.* **2011**, *13*, 262−266.

(35) Friebel, D.; Viswanathan, V.; Miller, D. J.; Anniyev, T.; Ogasawara, H.; Larsen, A. H.; O'Grady, C. P.; Nørskov, J. K.; Nilsson, A. *J. Am. Chem. Soc.* **2012**, *134*, 9664−9671.

(36) Safonova, O. V.; Tromp, M.; van Bokhoven, J. A.; de Groot, F. M. F.; Evans, J.; Glatzel, P. *J. Phys. Chem. B* **2006**, *110*, 16162−16164.

(37) Croy, J. R.; Mostafa, S.; Liu, J.; Sohn, Y.-h.; Roldan Cuenya, B. *Catal. Lett.* **2007**, *118*, 1−7.

(38) Ono, L. K.; Yuan, B.; Heinrich, H.; Roldan Cuenya, B. *J. Phys. Chem. C* **2010**, *114*, 22119−22133.

(39) Hübner, M.; Koziej, D.; Bauer, M.; Barsan, N.; Kvashnina, K.; Rossell, M. D.; Weimar, U.; Grunwaldt, J.-D. *Angew. Chem., Int. Ed.* **2011**, *50*, 2841−2844.

(40) Singh, J.; Alayon, E. M. C.; Tromp, M.; Safonova, O. V.; Glatzel, P.; Nachtegaal, M.; Frahm, R.; van Bokhoven, J. A. *Angew. Chem., Int. Ed.* **2008**, *47*, 9260−9264.

(41) Erickson, E. M.; Thorum, M. S.; Vasić, R.; Marinković, N. S.; Frenkel, A. I.; Gewirth, A. A.; Nuzzo, R. G. *J. Am. Chem. Soc.* **2012**, *134*, 197−200.

(42) Yoshida, H.; Nonoyama, S.; Yazawa, Y.; Hattori, T. *Phys. Scr.* **2005**, *T115*, 813−815.

(43) Russell, A. E.; Rose, A. *Chem. Rev.* **2004**, *104*, 4613−4635.

(44) Ichikuni, N.; Iwasawa, Y. *Catal. Lett.* **1993**, *20*, 87−95.

(45) Samant, M. G.; Boudart, M. *J. Phys. Chem.* **1991**, *95*, 4070−4074.

(46) Behafarid, F.; Ono, L. K.; Mostafa, S.; Croy, J. R.; Shafai, G.; Hong, S.; Rahman, T. S.; Bare, S. R.; Roldan Cuenya, B. *Phys. Chem. Chem. Phys.* **2012**, *14*, 11766−11779.

(47) Rehr, J. J.; Albers, R. C. *Rev. Mod. Phys.* **2000**, *72*, 621−654.

(48) You, H.; Zurawski, D. J.; Nagy, Z.; Yonco, R. M. *J. Chem. Phys.* **1994**, *100*, 4699−4702.

(49) Dam, V. A. T.; de Bruijn, F. A. *J. Electrochem. Soc.* **2007**, *154*, B494.